Energy Filtered Electron Tomography of Ice-Embedded Actin and Vesicles

Rudo Grimm,* Michael Bärmann,# Walter Häckl,# Dieter Typke,* Erich Sackmann,# and Wolfgang Baumeister*
*Max-Planck-Institut für Biochemie, Molekulare Strukturbiologie, D-82152 Martinsried, Germany, and #Physik-Department E 22, Technische Universität München, D-85748 Garching, Germany

ABSTRACT Semiautomatic single-axis tilt electron tomography has been used to visualize the three-dimensional organization of actin filaments in "phantom cells," i.e. lipid vesicles. The instrumentation consisted of a 120-kV electron microscope equipped with a postcolumn energy filter, which was used in the zero-loss imaging mode. Apart from changing the tilt angle, all steps required for automated tomography, such as recentering the image area, refocusing, and centering the energy-selecting slit, were performed by external computer control. This setup permitted imaging of ice-embedded samples up to a thickness of 800 nm with improved image contrast compared with that produced by tomography with a conventional electron microscope. In spite of the missing-wedge effect that is especially obvious in the study of membrane-filament interaction, single-axis tilt tomography was found to be an appropriate (in fact the only available) method for this kind of investigation. In contrast to random actin networks found in actin gels, actin filaments in and on vesicles with a bending radius of less than ~2 μm tend to be arranged in single layers of parallel filaments and often induce an elongated shape of the vesicles. Actin filaments located on the outside usually associate with the vesicle membrane.

INTRODUCTION

Embedding in vitreous ice has opened up new possibilities for imaging biological structures in a close-to-native state by electron microscopy (Dubochet et al., 1982). Recently the method has been applied in combination with energy filtering to macromolecular structures such as decorated actin filaments (Schröder et al., 1993) and ribosomes (Frank et al., 1995). Ice-embedded vesicles have been investigated in two dimensions (Lepault et al., 1985; Siegel et al., 1994) and in three dimensions by automated electron tomography (Dierksen et al., 1995). Whereas molecular structures are ideally embedded in ice less than 50 nm thick, larger structures not only need thicker ice but also may protrude out of an otherwise flat ice film (Grimm et al., 1996b). Vitrified vesicles and whole cells are typical structures that are embedded in an ice film thicker than 200 nm.

The vesicles portrayed in this paper are in the size range between 200 nm and 2 μm. The embedding ice is 100–500 nm thick, a thickness range in which unfiltered images are considerably blurred by inelastically scattered electrons. Zero-loss energy filtering removes all inelastically scattered electrons, thereby improving image quality (Schröder et al., 1990; Langmore and Smith, 1992; Grimm et al., 1996a). A typical example is shown in Fig. 1. A large vesicle with a diameter of 2 μm is recorded zero-loss filtered (Fig. 1 *a* and *b*) and unfiltered (Fig. 1 *c*) with a charge-coupled device (CCD) camera. The difference in observable image detail between the two images is clearly visible in areas where the ice is ~200 nm thick. Essentially no high-resolution information is left in the unfiltered image in areas thicker than 600 nm.

Here we investigate the relationship of actin filaments to the vesicle membrane. The vesicles were produced in a G-actin solution. After the swelling formation of the lipid membranes, the monomers were polymerized. We used these "phantom cells" as a model to evaluate the feasibility of visualizing macromolecular structures in a natural environment (see also O'Toole et al., 1993). To localize the actin filaments, one needs to know the three-dimensional structure of the vesicles. It can be obtained by automated single-axis tilt electron cryotomography as described by Dierksen et al. (1992; 1993). Automation is necessary to limit the electron exposure to the specimen to permit imaging of frozen-hydrated samples without damage. An in-depth discussion of the use of actin-containing vesicles in the study of actin–membrane interactions and a more detailed account of the vesicle preparation will be given in a separate publication (Bärmann et al., in preparation).

MATERIALS AND METHODS

Vesicle preparation

Dimyristoylphoshatidylcholine (DMPC) vesicles were prepared by electroswelling based on the method described by Dimitrov and Angelova (1987). A solution of DMPC containing 2.5% A23187 ionophore was applied onto two indium tin oxide–coated glass slides and thoroughly dried. These slides were inserted into a swelling chamber with the coated sides facing each other, held apart at a 0.5-mm distance by a Teflon spacer. The solution in the chamber contained 7 μM G-actin and 7 μM phalloidin in G-buffer (2 mM Tris/HCl, pH 7.5, 0.5 mM ATP, 50 μM $MgCl_2$, 0.2 mM DTT, 1 mM NaN_3) and was held at 30°C. An alternating field of 1 V at 10 Hz was applied to the slides for 2 h. After swelling, 7 μM DNAse I was added to prevent the polymerization of the actin outside the vesicles. Magnesium ions from a 100 mM $MgCl_2$ stock solution were added up to

Received for publication 22 August 1996 and in final form 21 October 1996.

Address reprint requests to Rudo Grimm, MPI Biochemie, Molekulare Strukturbiologie, D-82152 Martinsried, Germany. Tel.: 49-89-8578-2620; Fax: 49-89-8578-2641; E-mail: grimm@schubert.biochem.mpg.de.

0006-3495/97/01/482/08 $2.00

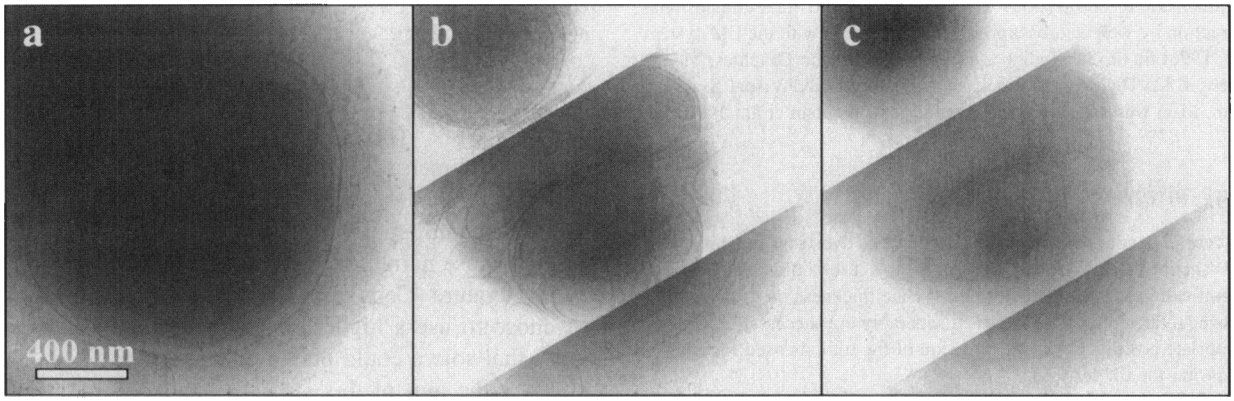

FIGURE 1 Contrast enhancement by zero-loss filtering in the image of a large vesicle (12,000× magnification). *a*, Unprocessed zero-loss filtered image. *b*, Same image as in *a* but divided into three regions to illustrate the full range of the CCD camera. *c*, Unfiltered image displayed in three regions. The approximate average specimen thickness was 200 nm in the lower right corner, 500 nm in the center, and 800 nm in the upper left corner. The dose for each image is ~200 electrons nm^{-2}, where only one or two electrons were collected in one CCD pixel in the upper left corner of the filtered image. Scaling was done by selection of similar regions from the images' histograms. The absolute scaling in CCD counts was 0–6000, 0–900, 0–100 for the filtered image and 2000–16,000, 2000–9000, and 2000–4000 for the unfiltered image. The conversion rate of the CCD camera was 27 counts per incident electron.

a final concentration of 2 mM to induce the polymerization of the actin inside the vesicles. The phalloidin was used to stabilize the filaments (Wieland, 1977). For electron microscopy, the solution containing the actin vesicles was then applied to holey carbon film upon a copper grid, blotted, and rapidly frozen in liquid ethane by use of an open plunging device (Dubochet et al., 1982). The grid was inserted into a Gatan cryoholder (Gatan Inc., Pleasanton, CA) and transferred into the microscope.

Electron microscopy

The setup of our energy-filtering microscope is shown in Fig. 2. The microscope, a CM 12 (Philips, Eindhoven, The Netherlands) was equipped with a standard eucentric goniometer (tilt range ±60°) connected to a digital angle readout with an accuracy of 0.1°. The goniometer was not interfaced to a computer, so the tilt angle had to be changed manually during the recording of a tomographic tilt series.

A postcolumn energy filter (Gatan Imaging Filter GIF 100; see Krivanek et al., 1995) was attached to the bottom flange of the viewing chamber of the microscope. The filter was equipped with a 14-bit 1024 × 1024 pixel slow-scan CCD camera with a P43 screen as the recording device. The

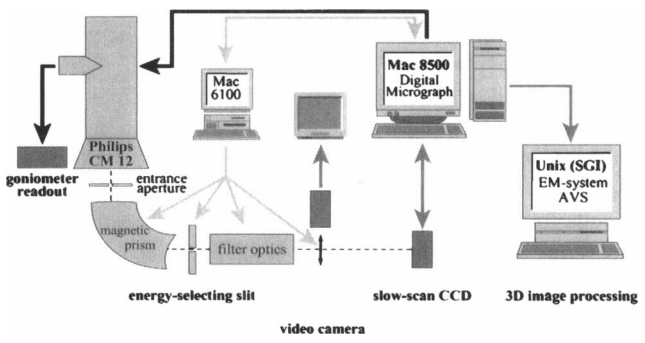

FIGURE 2 Setup of the filter microscope used for tomography. The microscope lenses are controlled by a (Power Macintosh) computer, whereas the goniometer tilt for every angle is (as yet) adjusted manually. The energy-selecting slit is electronically adjustable. Acquired images are later transferred and converted for processing by use of the EM system on a workstation.

count conversion rate of the slow-scan CCD camera was ~27 digits per incident electron. Low-dose imaging with the filter was done with two settings, corresponding to magnifications of 12,000× and 33,000× on the slow-scan CCD camera (Grimm et al., 1996a). The defocus was 5 μm unless otherwise stated. The microscope was controlled by Digital Micrograph 2.5 software (Gatan). After acquisition of a tomographic tilt series, images were transferred to a workstation for further image processing. A typical series took ~2 h to record and consisted of 59 images taken in 2° intervals from −58° to +58°. The actual tilt range was determined by the fact that an increasing area of the specimen grid is occluded from the electron beam by the rim of the head of the cryoholder with increasing tilt angle.

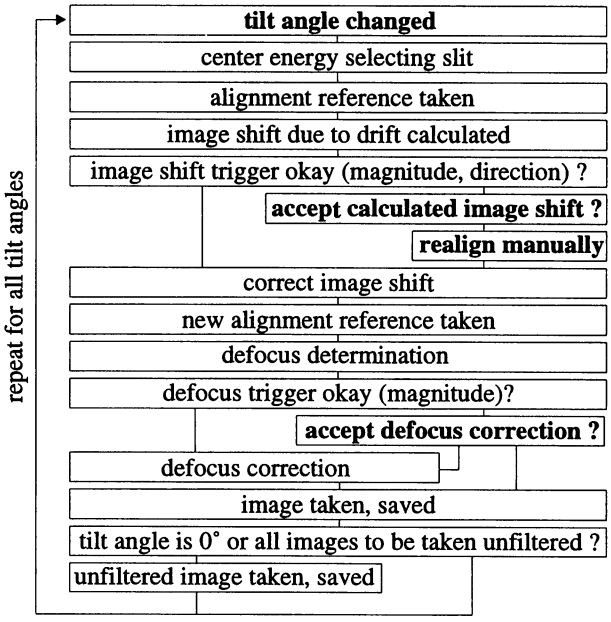

FIGURE 3 Repetitive part of a flow diagram of automated tomography. The procedures are fully automatic, except for the change of tilt angle. A trigger is used to detect unreasonable image shift or defocus measurements, in which case intervention by the user is required.

Alignment of the projections of the tilt series and three-dimensional reconstruction by weighted backprojection were done with the EM system (Hegerl, 1996) on an SGI Indigo 2 workstation (Silicon Graphics, Mountain View, CA). The program package AVS (Advanced Visual Systems, Waltham, MA) was used for surface rendering (Sheehan et al., 1996).

Energy-filtered electron tomography

Before data collection the sample is scanned at overview magnification (12,000× in our case). When an appropriate object for a tilt series is found, the magnification is increased. Because the ice thickness on grids holding large frozen hydrated samples varies considerably, it is necessary to choose an appropriate position along the direction of the tilt axis used for autofocusing during the tilt series.

The key steps of the tomography procedure are indicated in the flow diagram shown in Fig. 3. After the tilt angle is changed, we center the energy-selecting slit of the filter by taking a sequence of images at the focus position while changing the current in the filter's magnetic prism, thereby detecting one edge of the slit. The slit is set to a width of 10 eV, whereas the energy drift of the primary beam is 3–20 eV during a series. This energy shift is compensated for by adjustment of the magnetic prism instead of the high voltage because the response time of the magnetic prism is much faster. The total energy shift during a series is small enough not to affect the defocus measurably.

Autofocusing is performed by the beam-tilt method as described by Koster and de Ruijter (1992). Two images are taken to determine the defocus, and an additional image is used to correct for specimen drift. The accuracy of defocus correction by this method is within ±50 nm at 33,000× magnification (the pixel size at the specimen level is 0.73 nm for this magnification).

To permit computation of the specimen thickness by means of the log-ratio technique (Malis et al., 1988; Grimm et al., 1996b), the 0° projection is automatically recorded with and without an energy-selecting slit during a tomographic series.

Together with the acquired images, the microscope data, including the correction steps used when the tilt series is recorded, are saved. The data of a typical series are displayed in Fig. 4. Shown are image shifts perpendicular to the optical axis, the focus corrections, and the shifts of the primary beam energy. The tomography procedure is now implemented as an interpreted script with the Digital Micrograph software. For the alignment of the projections, a single gold cluster was used. A single cluster is sufficient for our purposes because the direction of the tilt axis had previously been determined from a tilt series of a carbon grid at room temperature by use of four gold markers (Lawrence, 1992). The final reconstructed volumes were obtained by 4 × 4 pixel binning (corresponding to a voxel size of 2.9 nm).

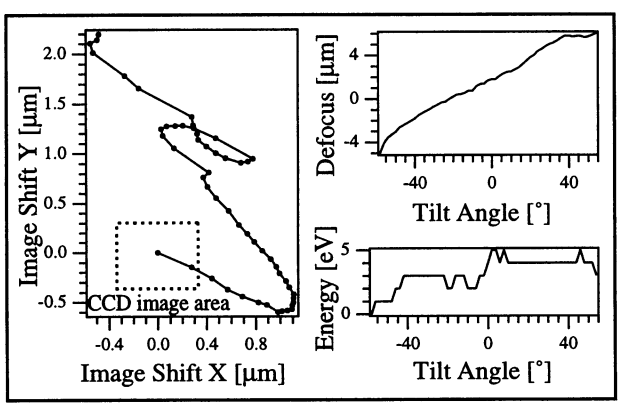

FIGURE 4 Plots of corrections for lateral shifts, focus, and energy shifts during recording of a tomographic series (shown in Fig. 5) from −58° to +54° in 2° increments at 33,000× magnification and 5-µm underfocus. The series was recorded in the zero-loss filtering mode.

RESULTS AND DISCUSSION

For our specimen we measured a threshold for bubbling of 50,000 to 130,000 electrons nm^{-2}, with substantially lower values for multilamellar vesicles and on the carbon support film. As these numbers are higher than previously reported in the literature (Conway et al., 1993; Frederik et al., 1993), we chose to use a higher dose for the tomographic series than usual so we could obtain an improved signal-to-noise ratio. As the aim of this study is the localization of actin filaments, the imaging conditions were chosen in such a way that small structural changes within the actin or in the lipid were not detected. Approximately 20% of the electron dose indicated for each series is used for alignment of the specimen area.

An example of a tilt series of actin-filled vesicles and its three-dimensional reconstruction is shown in Fig. 5. Several images from the tilt series are displayed in Fig. 5 *a*. For the reconstruction, the images are rotated in such a way that the tilt axis is parallel to the vertical side of the image. The surface-rendered model (Fig. 5 *g* and *h*) shows well-defined actin filaments oriented parallel to the elongated vesicles. Only the large vesicles, of which some are nested, contain visible actin filaments. Because of the r^3 law of the volume, vesicles of 20-nm diameter, for example, statistically contain fewer than two monomers. As the individual slices of the reconstruction show, the actin strands are most clearly visible on the upper and lower sides of the vesicles, whereas the vesicle membranes are best defined in the vicinity of the central *x*–*y* plane. This effect is due to the missing wedge in single-axis tilt tomography (see Hoppe and Hegerl, 1980; for the special case of vesicles see Dierksen et al., 1995) and because of it the top and bottom parts of the vesicle membrane are missing and the actin filaments near the central *x*–*y* plane, where they are directly on top of each other in the *z* direction, are fused. Fig. 6 shows a detail from the reconstruction in Fig. 5, where the actin is clearly seen inside the vesicle membrane. The filaments are oriented along the direction of elongation of the vesicle and are slightly inclined with respect to the *x*–*y* plane.

The parallel arrangement of actin filaments inside vesicles was also observed by light microscopy using polarizing filters (Miyata and Hotani, 1992), although in this case electrostatic interaction with negatively charged lipids may have been involved. Throughout our investigations we found this arrangement of filaments, in most cases combined with an elongated shape of the vesicles. On the light-microscopic scale, shape changes in vesicles owing to actin polymerization usually result in much more complex membrane deformation (Cortese at al., 1989; Bärmann et al., 1992). Because of the larger curvature of the vesicles observed in electron microscopy, the kinetics of filament formation is much more restricted, and the number of filaments that induce the change in shape is much smaller,

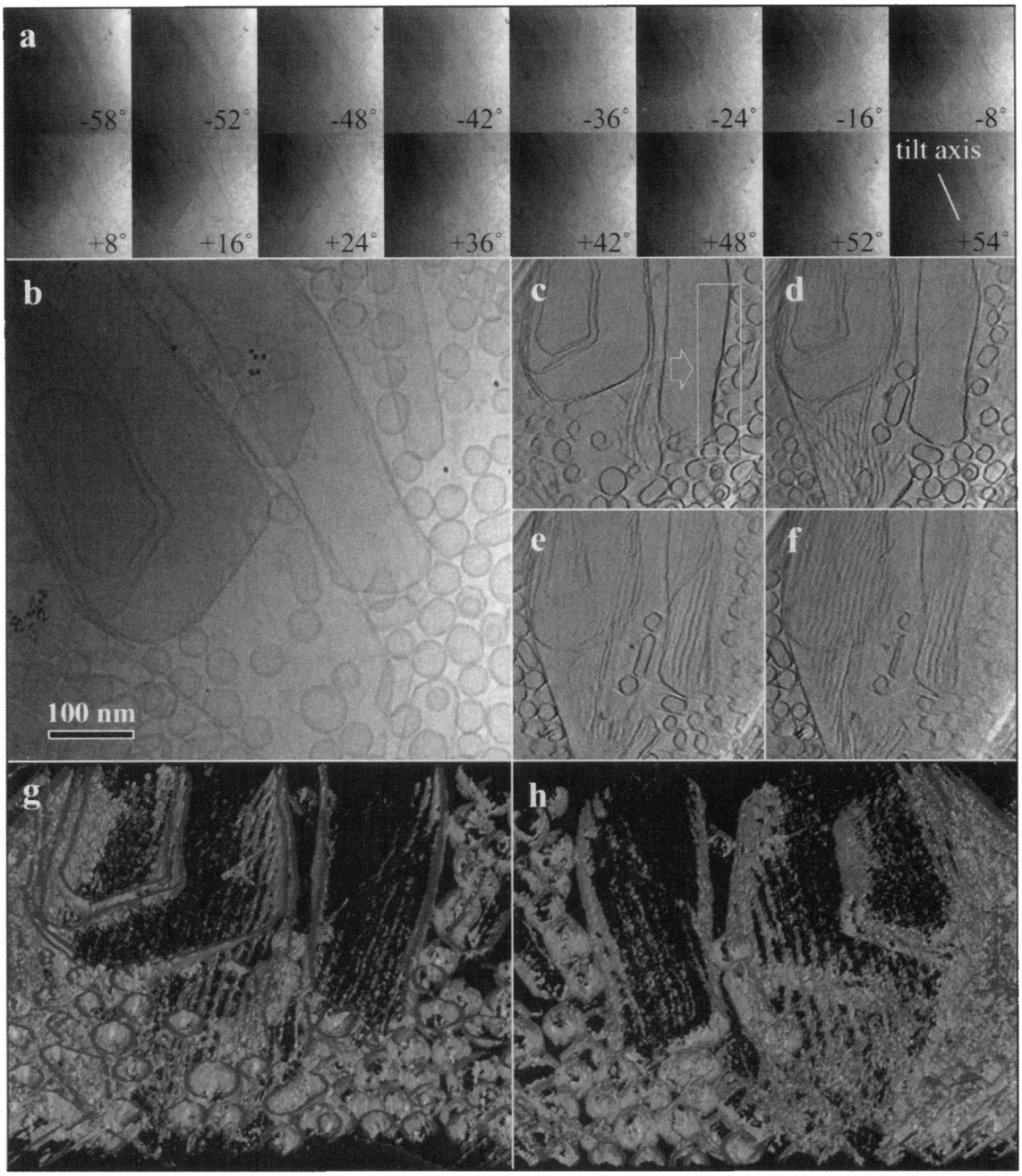

FIGURE 5 Actin filaments inside various vesicles. The specimen thickness ranges from 50 to 300 nm. The total dose used for the series was 20,000 electrons nm^{-2}. *a*, Gallery of selected views from the tomographic tilt series. *b*, Zero-loss filtered image at 0° tilt angle. *c–f*, Slices parallel to the *x–y* plane from the three-dimensional reconstruction, showing actin filaments and vesicle membranes. The slices are 3 nm thick and are located 0, 24, 38, and 47 nm, respectively, above the central plane. *g*, Surface rendering of the upper half of the reconstructed volume containing the slices shown in *c–f*. Same reconstruction as for *g* but viewed from below (rotated 180° about the *y* axis). *c–h* Have been rotated so that the tilt axis is parallel to the *y* axis. The area indicated in *c* is displayed in detail in Fig. 6.

20–50 for the vesicles shown in this paper. Additionally, phalloidin suppresses the dynamic equilibrium between G-actin and actin filaments—once formed—almost completely. Therefore no deformations more complex than elongation were observed.

An interesting question related to the resolving capacity of the method was whether it was possible to differentiate between filaments attached to the inside of the membrane and those attached to the outside. Figs. 7 and 8 display another reconstructed vesicle, in this case a tube several micrometers in length, for which actin filaments are found on the outer surface of the lipid bilayer. A comparison of the areas indicated by boxes in Fig. 7 *c* and *d* confirms this location of the filaments. There are clearly actin filaments

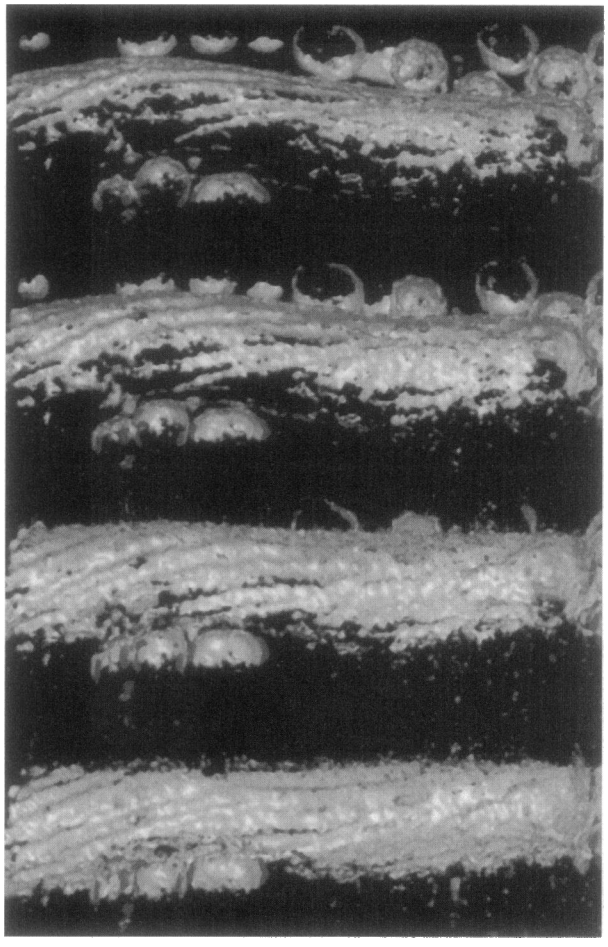

FIGURE 6 Detail from the data set displayed in Fig. 5 (as indicated in Fig. 5 *c*). The bottom picture shows the membrane as seen from a viewpoint inside the vesicle, viewed along the direction of the arrow in Fig. 5 *c*. The images above are tilted 20°, 40°, and 60° about the horizontal axis to give a three-dimensional impression of the geometry. The actin filaments are observed on the membrane in the bottom picture, extending into the region where no membrane is visualized because of the missing wedge in the top image.

running on the outer surface of the vesicle membrane on the right-hand side of Fig. 7 *c*, whereas the same membrane appears smooth on the inside (Fig. 7 *d*). An additional proof is provided by the filament indicated by the arrow in Fig. 7 *c*, which is pointing away from the membrane, while its lower end is on the vesicle. Actin filaments were always observed in close proximity to vesicles. This suggests that some actin monomers on the outsides of the vesicles were not inhibited by the DNAse and were subsequently polymerized just like the actin inside the vesicles in other cases. When no magnesium was added for polymerization we observed only spherical vesicles. Therefore the elongated vesicle shape, as shown, for example, in Fig. 7, must be induced by the actin filaments on the outside. The observation of "wagon train" shapes of elongated vesicles held by continuous actin filaments running in parallel (Fig. 9) supports this conclusion. As DMPC is a neutral lipid, there should be no electrostatic interaction between the actin monomers and the vesicles, and the reason for the actin attachment on the outside remains unclear. Electrostatic interaction has, however, been reported between actin and negatively charged surfaces (Weisenhorn et al., 1990) as well as between actin positively charged liposomes (Gicquault and Laliberté, 1988). For the case when the motion of the filaments is restricted to the membrane surface, theory predicts that the filaments will be arranged in parallel (Onsager, 1949).

The three-dimensional reconstruction of the actin network in Fig. 10 indicates the parallel orientation of the filaments in single layers on the membrane in another vesicle. In the 0° projection in Fig. 10 *b* we see the edge of an actin-filled vesicle and a well-defined mesh of filaments that does not seem to be contained by a visible membrane. The single slices of the reconstruction reveal the filaments inside the vesicle (*top row*, Fig. 10 *c*) as well as two populations of filaments in a structure on top of the vesicle (*bottom row*). One layer is running parallel to the *x* axis (*right*), and the other is inclined ~30° (*left*; *arrow*). The two orientations can best be distinguished in the first and the last images of the bottom row, whereas they are slightly mixed in the second and the third slices in the bottom row of Fig. 10 *c*. From the surface-rendered volume we can infer that this meshwork of filaments is actually contained in a flattened vesicle, where the top and the bottom membranes are brought into close proximity.

CONCLUSIONS

From the three-dimensional reconstructions of several vesicles containing actin we conclude that actin filaments inside electron-microscopically small vesicles, polymerized and stabilized with phalloidin, induce a deformation of the vesicles. Two-dimensional imaging and three-dimensional reconstructions of DMPC vesicles smaller than 2 μm in diameter reveal a parallel orientation of the filaments on the vesicle membrane. The individual filaments are 10–20 nm apart and form a well-ordered single layer (for a 7-μM initial actin monomer concentration). The parallel arrangement is independent of whether the filaments are located on the inner or the outer surface of the vesicle membrane. In both cases the filaments usually appear to be closely attached to the membrane and also often deform the vesicle to an elongated shape. As the filaments on the outside are in principle not limited in length, they often hold several vesicles linearly arranged like wagons of a train.

Automated electron tomography is currently the only available method for three-dimensional structure determination of unique objects at a molecular resolution. The method is limited mainly by the effect of the missing wedge, leading to ill-defined regions in the reconstruction of smooth surfaces. Tomography is possible with an energy filter as long as the energy-selecting slit can be recentered from time to time. The filtering provides a better signal-to-

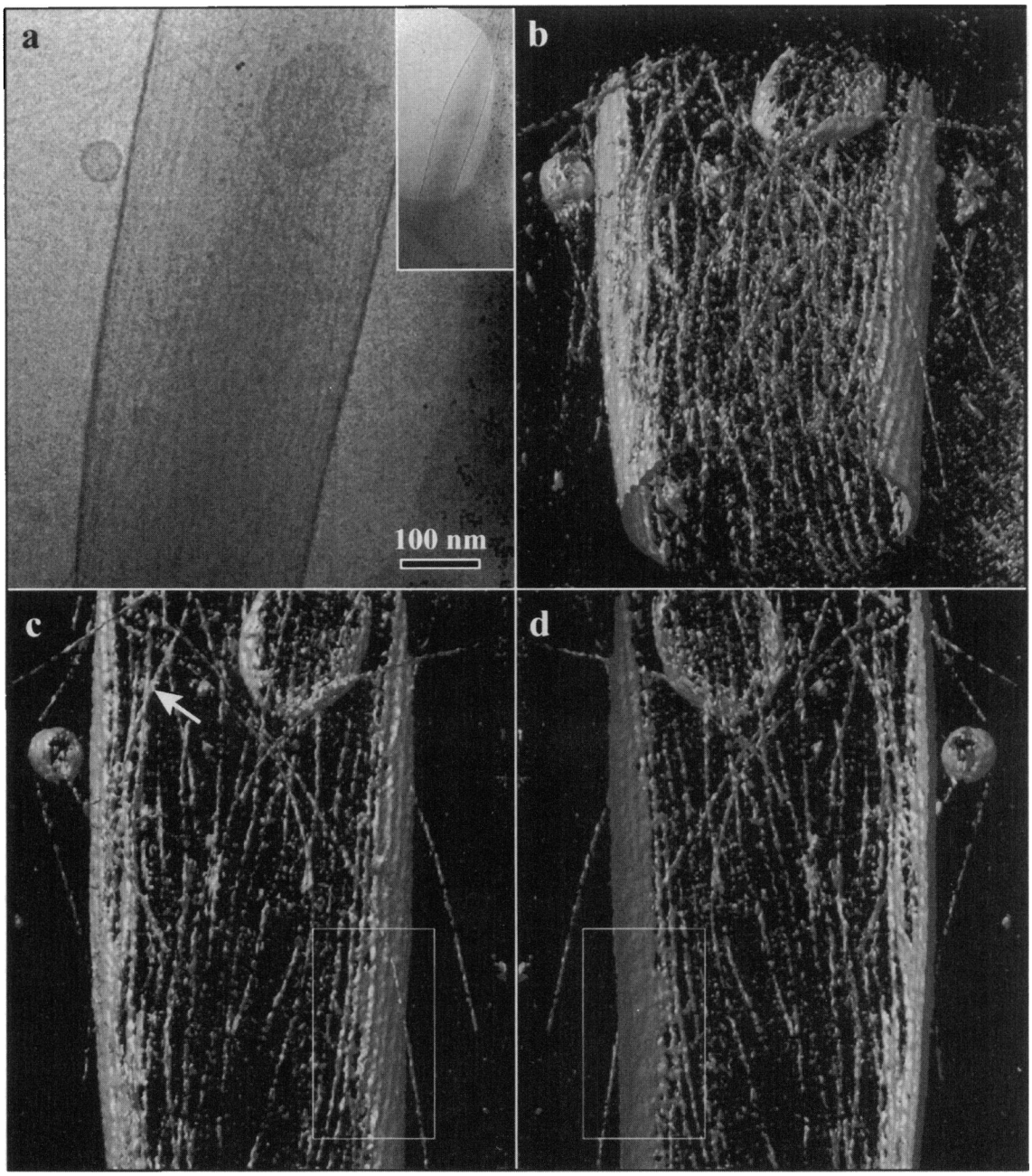

FIGURE 7 Long, hoselike vesicle and actin filaments (33,000× magnification, 5-μm underfocus, tilt angles $-56°$ to $+52°$, 15,000 electrons nm^{-2} total dose, 250-nm-thick ice). *a*, Projection at 0° tilt angle. The inset shows the vesicle at a lower magnification. *b*, Surface rendering of the reconstructed volume. The vesicle is slightly flattened. *c*, Upper half of the reconstruction in *b* as seen directly from the top. *d*, Same surface rendering as in *c* but viewed from below, to look at the membrane from the inside (rotated 180° about the *y* axis). Actin filaments are observed at some distance from the vesicle as well as attached to the membrane from the outside (*c*).

noise ratio in the images and therefore a better resolution in the final reconstructions.

We would like to thank Dr. A.J. Koster for helpful discussions about automated electron tomography and Dr. R. Hegerl, J. Walz, and A. Stoschek for the introducing R.G. to three-dimensional reconstruction techniques and denoising. We are grateful to the Deutsche Forschungsgemeinschaft for funding and to the Fonds der Chemischen Industrie for a doctoral fellowship awarded to R.G. The software scripts used for this and related work using Gatan's Digital Micrograph are available on the Internet on our energy filtering page at http://www.biochem.mpg.de/baumeister/EnergyFiltering.html.

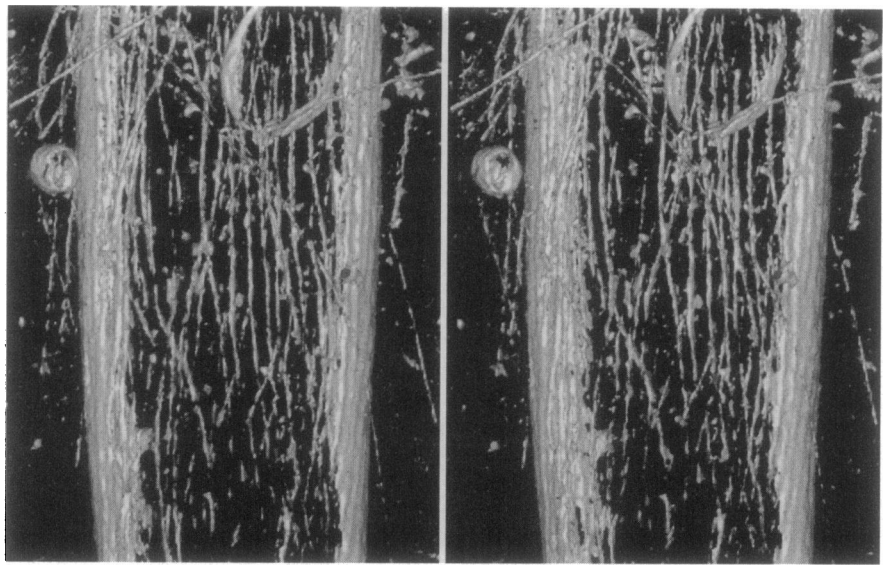

FIGURE 8 Stereo pair of the reconstructed volume displayed in Fig. 7 *b*. Denoising using a steerable pyramid algorithm (Stoschek et al., 1996) has been applied to facilitate the visibility of the single actin filaments on the top and the bottom of the vesicle. The denoising procedure smooths the appearance of the actin filaments on the vesicle membrane as shown in Fig. 7 *c*.

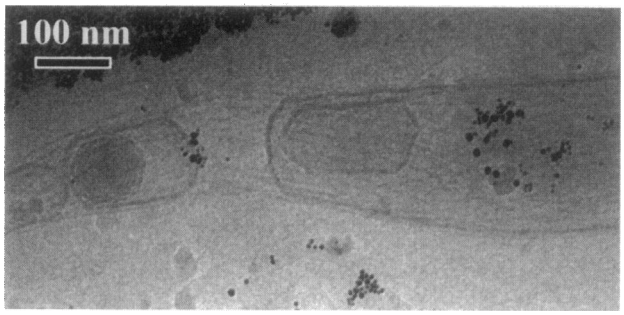

FIGURE 9 Gap between two elongated vesicles, which are held in line by actin filaments running on the outside. The two vesicles are part of a "wagon train," several micrometers long, consisting of ~10 vesicles.

REFERENCES

Bärmann, M., J. Käs, H. Kurzmeiser, and E. Sackmann. 1992. A new cell model—actin networks encaged by giant vesicles. *In* The Structure and Conformation of Amphiphilic Membranes, R. Lipowsky, D. Richter, and K. Kremer, editors. Vol. 66 of Springer Proceedings in Physics. Springer-Verlag, Heidelberg. 137–143.

Conway, J. F., B. L. Trus, F. P. Booy, W. W. Newcomb, J. C. Brown, and A. C. Steven. 1993. The effects of radiation damage on the structure of frozen hydrated HSV-1 capsids. *J. Struct. Biol.* 111:222–233.

Cortese, J. D., B. Schwab, C. Frieden, and E. L. Elson. 1989. Actin polymerization induces a shape change in actin-containing vesicles. *Proc. Natl. Acad. Sci. USA.* 86:5773–5777.

Dierksen, K., D. Typke, R. Hegerl, and W. Baumeister. 1993. Towards automatic electron tomography. II. Implementation of autofocus and low-dose procedures. *Ultramicroscopy.* 49:109–120.

Dierksen, K., D. Typke, R. Hegerl, A. J. Koster, and W. Baumeister. 1992. Towards automatic electron tomography. *Ultramicroscopy.* 40:71–87.

Dierksen, K., D. Typke, R. Hegerl, J. Walz, E. Sackmann, and W. Baumeister. 1995. Three-dimensional structure of lipid vesicles embedded in vitreous ice and investigated by automated electron tomography. *Biophys. J.* 68:1416–1422.

Dimitrov, D. S., and M. I. Angelova. 1987. Lipid swelling and liposome formation on solid surfaces in external electric fields. *Prog. Colloid Polymer Sci.* 73:48–56.

Dubochet, J., J. Lepault, R. Freeman, J. A. Berriman, and J.-C. Homo. 1982. Electron microscopy of frozen water and aqueous solutions. *J. Microsc.* 128:219–237.

Frank, J., J. Zhu, P. Penczek, Y. Li, S. Srivastava, A. Verschoor, M. Radermacher, R. Grassucci, R. K. Lata, and R. K. Agrawal. 1995. A model of protein synthesis based on cryo-electron microscopy of the *E. coli* ribosome. *Nature (London).* 376:441–444.

Frederik, P. M., P. H. H. Bomans, and M. C. A. Stuart. 1993. Matrix effects and the induction of mass loss or bubbling by the electron beam in vitrified hydrated specimens. *Ultramicroscopy.* 48:107–119.

Gicquault, C., and A. Laliberté. 1988. Polymerization of actin by positively charged liposomes. *J. Cell Biol.* 106:1221–1227.

Grimm, R., A. J. Koster, U. Ziese, D. Typke, and W. Baumeister. 1996a. Zero-loss energy filtering under low-dose conditions using a post-column energy filter. *J. Microsc.* 183:60–68.

Grimm, R., D. Typke, M. Bärmann, and W. Baumeister. 1996b. Determination of the inelastic mean free path in ice by examination of tilted vesicles and automated most probable loss imaging. *Ultramicroscopy.* 63:169–179.

Hegerl, R. 1996. The EM program package: a platform for image processing in biological electron microscopy. *J. Struct. Biol.* 116:30–34.

Hoppe, W., and R. Hegerl. 1980. Three-dimensional structure determination by electron microscopy. *In* Computer Processing of Electron Microscope Images. P. W. Hawkes, editor. Springer-Verlag, Heidelberg. 127–186.

Koster, A. J., and W. J. de Ruijter. 1992. Practical autoalignment of transmission electron microscopes. *Ultramicroscopy.* 40:89–107.

Krivanek, O. L., S. L. Friedman, A. J. Gubbens, and B. Kraus. 1995. An imaging filter for biological applications. *Ultramicroscopy.* 59:267–282.

Langmore, J. P., and M. F. Smith. 1992. Quantitative energy-filtered electron microscopy of biological molecules in ice. *Ultramicroscopy.* 46:349–373.

Lawrence, M. C. 1992. Least-squares method of alignment using markers. *In* Electron Tomography. J. Frank, editor. Plenum Publishing Co., New York. 197–204.

Lepault, J., F. Pattus, and N. Martin. 1985. Cryo-electron microscopy of artificial biological membranes. *Biochim. Biophys. Acta.* 820:315–318.

Malis, T., S. C. Cheng, and R. F. Egerton. 1988. EELS log-ratio technique for specimen-thickness measurement in the TEM. *J. Electron Microsc. Technol.* 8:193–200.

Miyata, H., and H. Hotani. 1992. Morphological changes in liposomes caused by polymerization of encapsulated actin and spontaneous formation of actin bundles. *Proc. Natl. Acad. Sci. USA.* 89:11,547–11,551.

Onsager, L. 1949. The effects of shape on the interaction of colloidal particles. *Ann. N.Y. Acad. Sci.* 51:627–659.

O'Toole, E., G. Wray, J. Kremer, and J. R. McIntosh. 1993. High voltage cryomicroscopy of human blood platelets. *J. Struct. Biol.* 110:55–66.

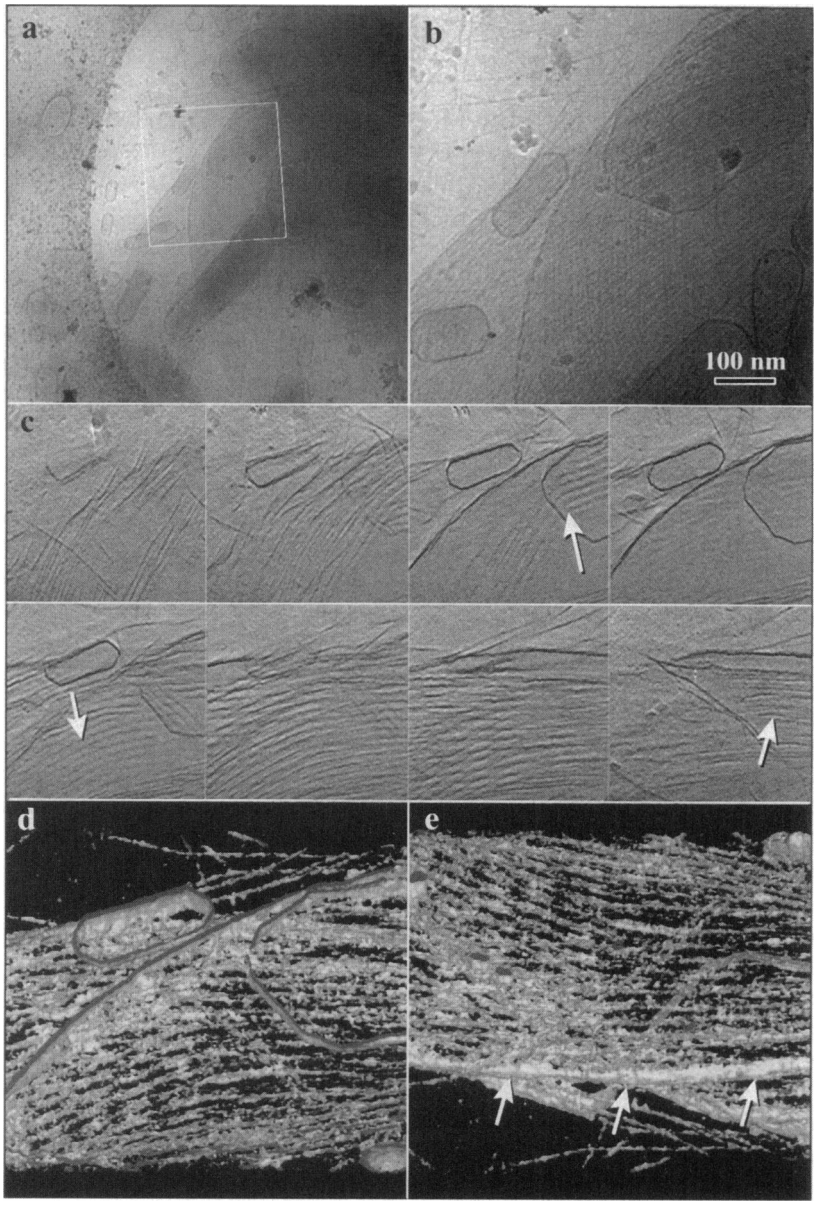

FIGURE 10 *a*, Assembly of vesicles and actin filaments at overview magnification. *b*, View of the area investigated by tomography (angular range −58° to +54° at 33,000× magnification, 90,000 electrons nm^{-2} total dose). A part of a large vesicle is observed on the right-hand side, whereas an actin meshwork that does not seem to be enclosed in a vesicle stretches diagonally from the lower left corner. *c*, Series of slices parallel to the *x*–*y* plane through the reconstructed volume. The individual slices are 3 nm thick and 15 nm apart. The first three slices show the actin network associated with the large vesicle on the right, which is apparently deformed in the vicinity of the smaller enclosed vesicle on the right-hand side (*arrow*). The last four slices show a dense actin network, which displays the typical parallel ordering of the filaments. The arrows indicate two sets of filaments inclined ~40° with respect to each other. *d*, Surface rendering of the top half of the reconstructed volume containing the large meshwork as seen from the inside of the large vesicle. *e*, The same surface rendering viewed from the top, i.e., rotated 180° about the *x* axis relative to *d*. The meshwork displays a well-defined edge at the front, which appears to be the continuous membrane of a flattened vesicle (*arrows*). As this vesicle is extremely flat, it does not show up clearly in the original projection image (*b*).

Schröder, R. R., W. Hofmann, and J.-F. Ménétret. 1990. Zero-loss energy filtering as improved imaging mode in cryoelectronmicroscopy of frozen-hydrated specimens. *J. Struct. Biol.* 105:28–34.

Schröder, R. R., D. J. Manstein, W. Jahn, H. Holden, I. Rayment, K. C. Holmes, and J. A. Spudich. 1993. Three-dimensional atomic model of F-actin decorated with *Dictyostelium* myosin S1. *Nature (London).* 364:171–174.

Sheehan, B., S. D. Fuller, M. E. Pique, and M. Yeager. 1996. AVS software for visualization in molecular microscopy. *J. Struct. Biol.* 116:99–106.

Siegel, D. P., W. J. Green, and Y. Talmon. 1994. The mechanism of lamellar-to-inverted haxagonal phase transitions: a study using temperature-jump cryo-electron microscopy. *Biophys. J.* 66:402–414.

Stoschek, A., T. P. Y. Yu, and R. Hegerl. 1996. Rotation-invariant and robust multiple-2D-object detection using steerable pyramid denoising and optimized circular harmonic filters. *In* Proceedings of the 13th International Conference on Pattern Recognition. Vol. II, Track B, 376–380. IEEE Computer Society Press, New York.

Weisenhorn, A. L., B. Drake, C. B. Prater, S. A. C. Gould, P. K. Hansma, F. Ohnesorge, M. Egger, S.-P. Heyn, and H. E. Gaub. 1990. Immobilized proteins in buffer imaged at molecular resolution by atomic force microscopy. *Biophys. J.* 58:1251–1258.

Wieland, T. 1977. Modifications of actins by phallotoxins. *Naturwissenschaften.* 64:303–309.